Inverter Loss Reduction Method of Air Conditioners With Adjustable DC-Link Voltage Control and Six-Step Operation

Jisun Ham, *Student Member, IEEE*, Hwigon Kim, *Member, IEEE*, Junyeol Maeng, *Student Member, IEEE*, and Shenghui Cui, *Member, IEEE*

***Abstract*—This article proposes a control method for a two-stage power conversion system of a residential air conditioner drivetrain to enhance power density and reduce the hardware cost of the converters. In hardware design, the heatsink is determined based on the rated operating point, where the maximum loss occurs. When the motor operates at its rated operating point, the converter loss can be minimized using six-step operation. Compared to the existing six-step operation methods to reduce switching device losses, the proposed control method utilizes the dc-link voltage and the phase angle of the voltage vector as 2 degrees of freedom for control, which enables independent control of the *dq*-axis current, thus enabling optimal operation, such as maximum torque per ampere. However, in the low-speed operation region, where efficiency is critical for the energy efficiency grade, linear modulation should be applied. The proposed method addresses a seamless transition between linear modulation in light load and six-step operation in heavy load. The validity of the proposed method is verified through experiments on a 7 kW drivetrain system of a residential air conditioner.**

***Index Terms*—Boost-type power factor correction (PFC), inverter-based air conditioner, motor drives, overmodulation, six-step operation, variable dc-link, vector control.**

I. Introduction

With the growing concern about energy consumption and utilization, energy standard requirements for home appliances are also being tightened [1]. Recently, research has been actively underway in the field of home appliances to achieve high efficiency and high power-density inverter-based air conditioners [2], [3]. The inverter-based air conditioners have unique operating profiles as follows: they perform rated power operation during the initial startup to reach the target air temperature as fast as possible. Given the nature of the fluid load, rated power operation means that the compressor motor operates at rated speed and torque. After initial startup, the compressor motor operates at a sufficiently low speed at light loads for the remainder of the mission profile to sustain the target air temperature. Therefore, due to the operational characteristics of the inverter-based air conditioner, the air conditioner operates at a higher percentage of service time in light loads compared to heavy loads [4]. Consequently, optimizing light-load efficiency becomes paramount for a better energy efficiency grade.

On the other hand, the ratings of switching devices and heatsink design are determined by heavy-load conditions. In variable-speed compressor motor drives, due to the nature of fluid load, the highest energy losses occur during the rated operation of the motor, where the motor presents the maximum speed and torque simultaneously. Therefore, to minimize the heatsink size, the main goal is to reduce the total losses of the switching devices when the compressor motor operates at full speed.

Since residential air conditioners are connected to the ac mains and operate at variable speeds, they typically consist of two power conversion stages. Unlike single-stage power converters, two-stage power converters offer the flexibility to vary the dc-link voltage. For a two-stage power conversion system, control methods using variable dc-link voltage have been proposed to reduce switching device losses [5], [6], [7], [8], [9]. In [5], [6], [7], and [8], studies have been conducted on the electric vehicle drivetrain, which adds a dc–dc converter between the battery and the dc-link of the inverter. In these literatures, the dc-link voltage of the inverter is varied by the dc–dc converter to improve the overall performance of the drivetrain. In [5], [6], and [7], a dc–dc converter is used to optimize the inverter dc-link voltage to maximize the operating area that can be driven by maximum torque per ampere (MTPA) operation, thereby reducing the conduction losses of the system. In [8], a buck converter is used to control the dc-link voltage in order to maximize the modulation index (MI) and lower the total harmonic distortion (THD). In [9], the light-load efficiency of the air conditioner drivetrain is improved by lowering the dc-link voltage under light-load conditions. The dc-link voltage reference is determined by a discrete value without any formulaic criteria. In summary, previous research [5], [6], [7], [8], [9] has leveraged the dc-link voltage to reduce converter losses. However, in the context of residential air conditioners, which are constructed with a boost-type power

Received 8 June 2025; revised 22 September 2025; accepted 26 October 2025. Date of publication 3 November 2025; date of current version 19 January 2026. This work was supported by the Technology Innovation Program (or Industrial Strategic Technology Development Program under Grant RS-2024-00432085, Development of Control System for High Power Medium-Voltage Drive based on Modular Multilevel Converter) funded By the Ministry of Trade, Industry and Energy (MOTIE, South Korea). Recommended for publication by Associate Editor G.-S. Seo. *(Corresponding author: Shenghui Cui.)*

The authors are with the Department of Electrical and Computer Engineering and SNU Electric Power Research Institute, Seoul National University, Seoul 08826, South Korea (e-mail: wltjs917@snu.ac.kr; hwigon@eepel.snu.ac.kr; junyul7@snu.ac.kr; cuish@snu.ac.kr).

Color versions of one or more figures in this article are available at https://doi.org/10.1109/TPEL.2025.3627960.

Digital Object Identifier 10.1109/TPEL.2025.3627960

TABLE I
SUMMARY OF VARIABLE DC-LINK VOLTAGE CONTROL APPROACHES FOR TWO-STAGE POWER CONVERSION SYSTEMS

References	Variable V_{dc}	Heavy-load loss ↓	V_{dc} as DoF in closed-loop current control	Seamless transition
[5], [6], [7], [8], [9],	O	X	X	X
[12]	O	O	X	X
[13]	O	O	X	X
[14]	O	O	X	X
Proposed (this work)	O	O	O	O

factor correction (PFC) circuit, reduction of switching loss by lowering the dc-link voltage is not feasible. Moreover, the works presented in [5], [6], [7], [8], and [9] focus on the reduction of losses in light- and medium-load conditions, but the heavy-load losses at the rated speed of the motor still remain high.

Another method to reduce the switching device losses in an inverter is the six-step operation. The six-step operation offers the significant advantage of effectively reducing switching losses, thanks to the switching frequency as low as the fundamental frequency of the motor. Furthermore, conduction losses can also be minimized by maximizing the output voltage magnitude and reducing excessive currents during flux-weakening operation [10], [11]. Advanced control methods have been proposed to reduce switching device losses by utilizing variable dc-link voltage and applying six-step operation [12], [13], [14]. In [12], an active-front-end inverter connected to a permanent magnet synchronous generator is used to regulate the output power. In this article, dc-link voltage is controlled to operate the inverter in six-step mode to reduce switching losses. However, due to limited dynamics in controlling the dc-link voltage, the output power is regulated in a very limited bandwidth. In [13], a control method is proposed for motor drive application, where the torque is controlled by adjusting the phase angle of the switching pulse during the six-step operation. This torque control method operates in a closed loop, utilizing a torque observer to mitigate stability issues compared to [12]. However, this method exhibits a slow dynamic characteristic because the dc-link voltage is not used as a degree of freedom for the inverter output voltage control. In [14], the dc-link voltage and the inverter output voltage angles are simultaneously controlled to regulate the output torque in six-step operation at high speeds. Therefore, it is possible to improve the torque control dynamics and reduce the torque ripple. However, in the studies above, the output torque is controlled by the stator flux angle not the motor current, which is not directly controlled. Such approaches complicate the prevention of over current in both the motor and inverter, and MTPA method cannot be applied to reduce conduction losses in low-speed operation. This limitation primarily stems from the dc-link voltage not being utilized as a degree of freedom in current control. Table I summarizes prior methods against four criteria and highlights a consistent gap: the dc-link voltage is rarely used as a closed-loop current control degree of freedom.

By performing the six-step operation, switching device losses can be reduced. However, due to the nature of residential air conditioners operating with boost-type PFCs, there is a minimum value of the dc-link voltage. If the six-step operation is applied at low speeds, the dc-link voltage cannot be lowered below this minimum value, leading to flux enhancement and degradation of motor and inverter efficiency. Note that efficiency is critical at light load, so linear modulation should be employed. Therefore, it is necessary to perform linear modulation at low speeds and six-step operation at high speeds. Linear modulation allows accurate voltage synthesis, while six-step can only synthesize a fixed voltage magnitude. Given the differences between the two operations, a seamless transition is required to effectively cover all operating areas, which has not been thoroughly investigated in the existing literature [12], [13], [14].

This article proposes a motor control method for the air conditioner drivetrain, where the dc-link voltage is controlled by a grid-side PFC converter. To reduce switching device losses, the proposed control method utilizes two control degrees of freedom—the dc-link voltage and the inverter output voltage angle—to independently control the dq-axis currents in six-step operation with heavy load conditions of the motor drive. The proposed method exhibits fast motor current control dynamics and is robust against motor parameter errors, such as resistance and inductance variations, compared to the conventional method that regulates output torque with the flux angle. While reducing switching losses at high speeds is important, linear modulation at light loads is necessary because light-load efficiency is a crucial focus in home appliances. Accordingly, the proposed method operates with linear modulation at low speed and switches to six-step at high speed, leveraging the variable dc-link voltage for accurate voltage synthesis in six-step mode. To bridge the gap between linear modulation and six-step operation, overmodulation is applied in between to enable accurate fundamental voltage synthesis to assure successful closed-loop current control of the motor during mode transition with the motor speed. The contribution of this work lies not in the use of six-step modulation itself, but in its integration into a practical control framework that minimizes power losses and enables seamless transitions among modulation modes.

The rest of this article is organized as follows. Section II describes the operating profile and control structure of the electric drivetrain in the residential air conditioner, providing a baseline for conventional operation. In Section III, details of the proposed control method taking advantage of variable dc-link voltage are elucidated. This section includes three key strategies: dq-axis current control using variable dc-link voltage, seamless mode transition, and overmodulation for continuous voltage synthesis. Section IV presents the experimental results of the proposed control method. The results validate the effectiveness of the proposed control method. Finally, Section V concludes this article.

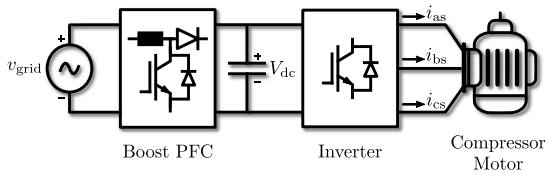

Fig. 1. Electric drivetrain of air conditioners.

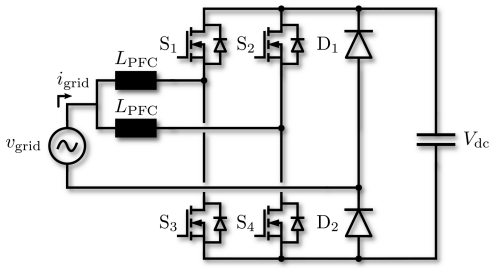

Fig. 2. Interleaved totem-pole PFC topology.

This article follows its conference version [15] with substantial improvements, including the following.

1) Analysis on the impact of the presence of overmodulation during operation mode transition and methodology of seamless mode transition.

2) Practical control considerations for six-step operation, including flux-weakening operation based on dc-link voltage information and a method to eliminate voltage phase angle error in digital implementation.

3) A power feedforward-based dc-link voltage control with a sixth-harmonic notch filter is introduced to enhance the dynamic response of voltage regulation, and grid code compliance is experimentally verified in the PFC stage.

4) Experimental validation and detailed loss breakdown under practical air-conditioner drive profiles.

II. Control of Electric Drivetrain in Existing Air Conditioners

Fig. 1 shows the electric drivetrain diagram of air conditioners in the industry. It consists of a PFC circuit, an inverter, and a compressor motor. In this configuration, the PFC receives input from the grid and converts ac to dc. The inverter at the rear stage controls the motor. Therefore, the electric drivetrain in the air conditioner feeds the compressor motor through PFC and inverter control.

A. PFC Converter

It is crucial to ensure that electric drivetrain can be connected to the grid while complying with grid harmonics regulations set forth by the International Electrotechnical Commission (IEC). Household air conditioners are typically with power ratings in the range of several kWs, therefore, the Class A criteria of regulation IEC 61000-3-2 should be met. PFC circuits are used as the front end to comply with harmonic regulations.

Typically, boost-type PFC circuits are employed in air conditioners and the bridge-less boost-type PFC depicted in Fig. 2

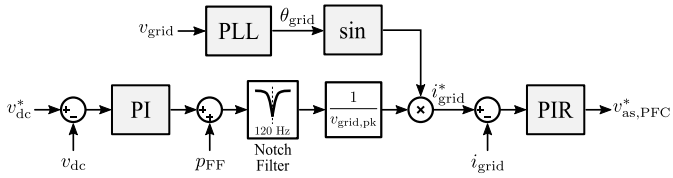

Fig. 3. Block diagram of PFC controller.

is employed in the drivetrain of the air conditioner investigated in this article. Given the nature of fluid loads, the torque of a motor is proportional to the square of its rotational speed. As the load increases, the voltage required to control the motor speed also increases. With boost-type PFCs, it is possible to boost the dc-link voltage to extend the operating region of the motor. But the dc-link voltage cannot be lower than the voltage where the ac power source is rectified by a diode bridge. With a 220 V single-phase main, the minimum dc-link voltage, $V_{\text{dc,min}}$, is 311 V.

Fig. 3 shows the control block diagram of the PFC. An outer loop employs a proportional–integral controller to control the dc-link voltage, and an inner loop utilizes a proportional–integral–resonant controller to control the grid current. The load power p_{FF} is feedforwarded to improve the dynamics of dc-link voltage control. In addition, a notch filter is used to minimize the effect of the second-order harmonic component of power reference results from the nature of single-phase system. To regulate the power factor, a phase-locked loop is utilized to estimate the phase angle and frequency of the grid voltage.

B. Inverter

Fig. 4(a) shows the typical operation scheme of an inverter with a boost-type PFC in air conditioners. In the figure, linear modulation (LM), overmodulation (OVM), and flux-weakening (FW) operation. In such drive systems, the LM region is typically implemented using space vector pulsewidth modulation to ensure low current ripple and high efficiency under light-load conditions. Since a boost-type PFC is placed at the front stage, the dc-link voltage, V_{dc}, can be adjusted. When the synthesizable voltage of the inverter is higher than the motor voltage, V_{dc} is maintained at the minimum value $V_{\text{dc,min}}$, to minimize switching losses in both the inverter and the PFC. As the motor speed keeps increasing, the motor voltage magnitude exceeds the maximum inverter output voltage in the linear region, namely $(1/\sqrt{3})V_{\text{dc,min}}$. Therefore, V_{dc} is boosted by PFC accordingly to widen the operating speed of the motor. In this case, the maximum dc-link voltage $V_{\text{dc,max}}$ is limited by system design parameters, such as rated voltage of the switching devices and dc-link capacitor. When the dc-link voltage is saturated at its maximum value $V_{\text{dc,max}}$, overmodulation is performed to extend the output voltage further in order to increase the speed. When overmodulation reaches the maximum voltage synthesis capability, flux-weakening operation ensues.

Fig. 5 shows the block diagram of the inverter control unit [16]. In the motor control, the speed controller generates the torque reference T^*. Then, the d and q-axis current references of

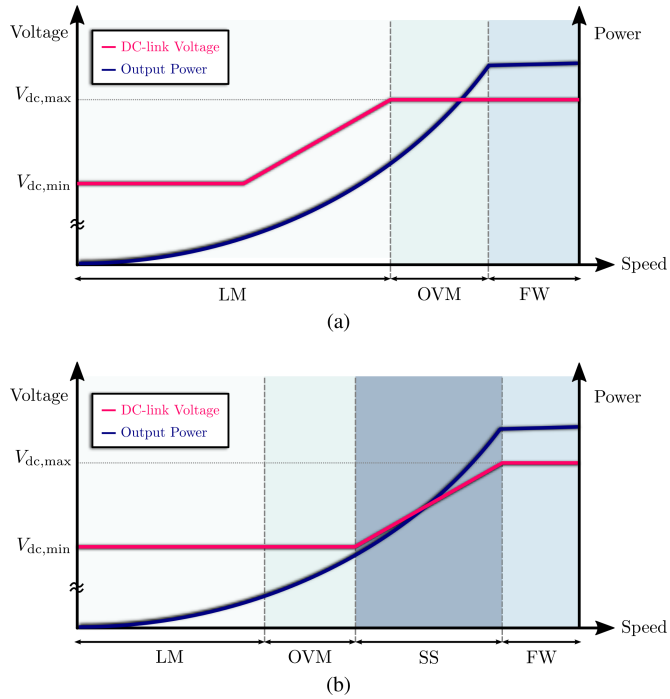

Fig. 4. Operation scheme of inverter with boost-type PFC for compressor motor drive in air conditioners. (a) Conventional method. (b) Proposed method.

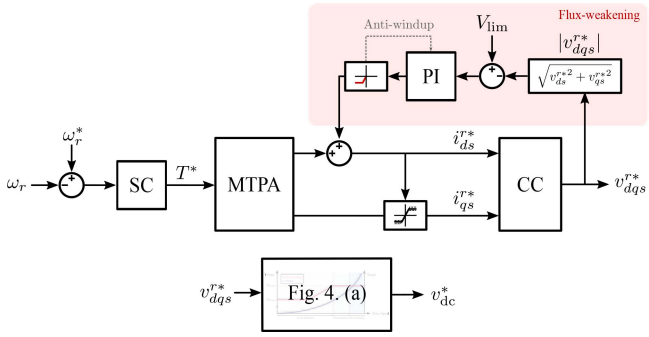

Fig. 5. Block diagram of conventional inverter controller.

motor i^{r*}_{dqs} are generated through the MTPA look-up table, which takes the torque reference as its input. The current controller (CC) generates the inverter output voltage reference v^{r*}_{dqs} based on the d and q-axis current errors. As shown in the figure, the speed of the motor ω_r determines T^* and v^{r*}_{dqs} determines $v^*_{\rm dc}$. At low speeds, linear modulation is performed which synthesizes accurate fundamental voltage. As the speed of the motor increases, overmodulation, and flux-weakening operation ensue when linear modulation is unattainable. The transition from overmodulation to flux-weakening operation is determined by the value of $V_{\rm lim}$. $V_{\rm lim}$ is the limiting value of the magnitude of the synthesized voltage reference $|v^{r*}_{dqs}|$. Taking into account the margin and the ripple component introduced to the $|v^{r*}_{dqs}|$ by the motor current harmonic, $V_{\rm lim}$ is set to approximately $0.95V_{\rm dc}$ [17]. Overmodulation occurs when $|v^{r*}_{dqs}|$ exceeds $(1/\sqrt{3})V_{\rm dc}$ but remains below $V_{\rm lim}$. If the motor output voltage reference exceeds the limiting value $V_{\rm lim}$, the flux-weakening operation is performed.

III. Proposed Control Method

Fig. 4(b) shows the proposed operation scheme of an inverter with boost-type PFC. In the figure, SS represents six-step operation. In the proposed method, LM and OVM are performed with $V_{\rm dc,min}$, and SS is performed with a variable dc-link voltage under $V_{\rm dc,max}$. When the dc-link voltage reaches maximum dc-link voltage, $V_{\rm dc,max}$, FW control is executed.

In the conventional method, as shown in Fig. 4(a), LM is performed with $V_{\rm dc,min}$ and boosted voltage. In contrast, the proposed method only performs LM with $V_{\rm dc,min}$, and when the required synthesized voltage becomes larger, OVM is performed. Therefore, the proposed method has less switching loss, unlike the conventional method, which uses boosted dc-link voltage. When a larger voltage needs to be synthesized, the conventional method performs OVM and further performs FW. In the proposed method, SS is performed with variable dc-link voltage. When the dc-link voltage cannot be boosted up further, FW is performed. By performing SS rather than OVM, switching losses can be significantly reduced. In the case of FW, the proposed method utilizes the maximum synthesized voltage, resulting in fewer losses.

A. Six-Step Operation With Variable DC-Link Voltage

The magnitude of the motor output voltage can be represented by

$$|v^r_{dqs}| = \sqrt{{v^r_{ds}}^2 + {v^r_{qs}}^2} \approx \omega_r \sqrt{(L_q i^r_{qs})^2 + (L_d i^r_{ds} + \lambda_f)^2}. \quad (1)$$

In the equation, λ_f represents the magnet flux and L_d and L_q are the stator d and q-axis inductance, respectively. Stator resistance is not considered in this equation to simplify the analysis. As shown in the equation, the motor output voltage is a function of motor speed and stator current. The fundamental output voltage synthesized by the inverter in SS is given by

$$|v^r_{dqs}| = \frac{2}{\pi} V_{\rm dc}. \quad (2)$$

As shown in the equation, the magnitude of the synthesized voltage during SS is proportional to the dc-link voltage. In this article, the control method is proposed to synthesize the required output voltage exactly using a variable dc-link voltage in SS. Therefore, the proposed method can provide closed-loop current control of the motor, as in the linear modulation. In the proposed control method with SS, dc-link voltage is varied and utilized as an additional degree of freedom for current control in conjunction with the selection of the voltage vector. Hence, independent d and q-axis current control is achieved and accurate voltage synthesis is possible even in SS. The structure of the proposed control method is depicted in Fig. 6. In the proposed method, the controller for SS is implemented by considering the following four features: $V^*_{\rm dc}$ calculation, flux-weakening operation, power feedforward, and sawtooth carrier-based implementation of SS.

1) V^*_{dc} Calculation: The magnitude of the synthesized voltage in SS can be expressed in terms of the dc-link voltage, allowing for the calculation of the required dc-link voltage

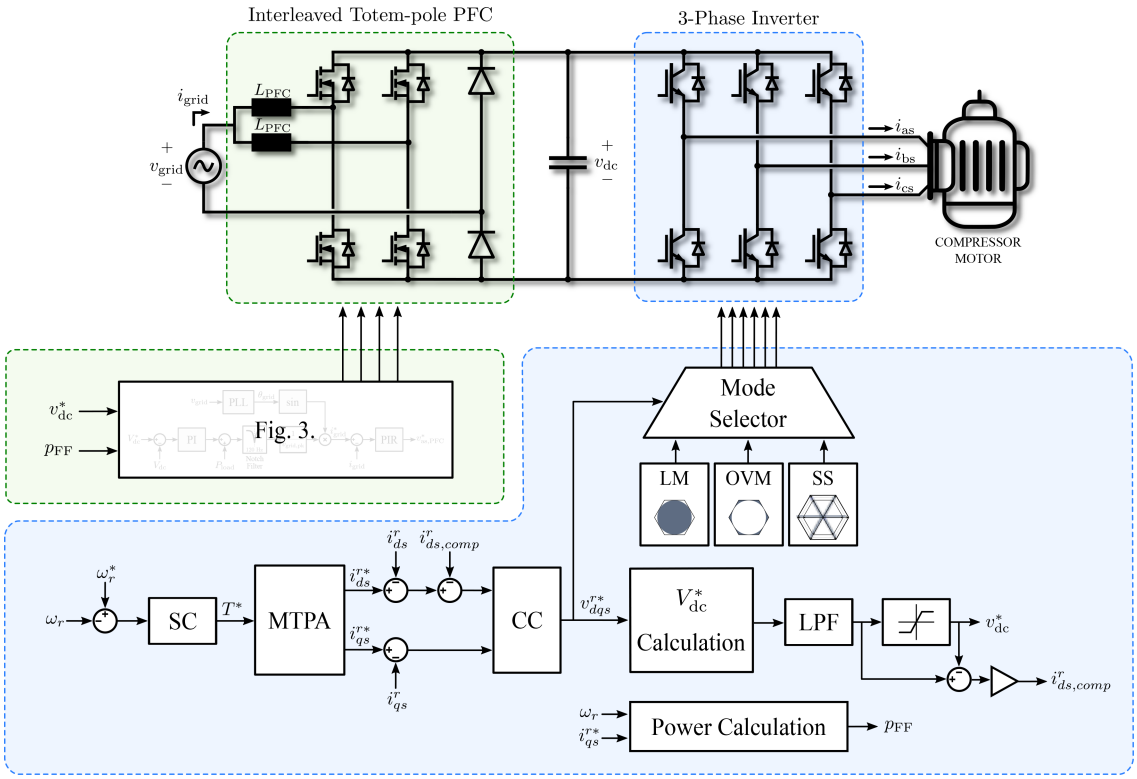

Fig. 6. Block diagram of proposed control method.

magnitude. Accordingly, the dc-link voltage reference in SS is determined by

$$V^*_{\rm dc} = |v^{r*}_{dqs}| \times \frac{\pi}{2}. \tag{3}$$

If the calculated dc-link voltage reference $V^*_{\rm dc}$ is less than the grid rectified voltage, $V_{\rm dc,min}$, it is saturated at $V_{\rm dc,min}$, and if it is greater than the maximum voltage, $V_{\rm dc,max}$, it is saturated at $V_{\rm dc,max}$.

2) Flux-Weakening Operation: When driving a motor, both the current limit and voltage limit should be satisfied. To maximize the operational speed of the motor within these conditions, flux-weakening operation is carried out. Conventional flux-weakening operation compensates for the error in voltage synthesis when the reference voltage is larger than the synthesizable voltage. This is done by applying saturation to the phase voltage reference $|v^{r*}_{dqs}|$.

However, in the proposed method, accurate voltage synthesis is achieved to realize closed-loop current control even in SS. Therefore, saturation is applied to the dc-link voltage reference $V^*_{\rm dc}$, not the phase voltage reference v^{r*}_{dqs}. If $V^*_{\rm dc}$ is larger than the limit $V_{\rm dc,max}$, there will be an error between the reference and the synthesized voltage. In this case, the flux-weakening operation is performed by applying saturation to the dc-link voltage reference $V^*_{\rm dc}$ and compensating for the difference between the two values as $i^r_{\rm ds,comp}$, which is the demagnetization current applied in the d-axis. This approach allows for better utilization of the available voltage compared to conventional flux-weakening methods, thereby requiring a smaller d-axis current for maintaining the desired torque.

3) Power Feedforward: The dc-link voltage is controlled by PFC, and the control bandwidth should be sufficiently high for effective dc-link voltage control in SS. Therefore, to ensure sufficient dynamics, the inverter output power is calculated and feedforward to the dc-link voltage controller in the PFC. If the measured q-axis current i^r_{qs} is used to calculate the power, the resulting power calculation includes a sixth-order harmonic component of the angular frequency. To avoid this, the feedforward power $p_{\rm FF}$ is calculated using the reference value of the q-axis current i^{r*}_{qs}.

4) Sawtooth Carrier-Based Six-Step Operation: When the inverter operates in SS with a digital controller, a voltage phase angle error between the synthesized voltage and the actual voltage could occurs if the sampling frequency is not high enough. When such phase angle errors occur, undesirable harmonics are generated in the motor current, leading to torque ripple and audible noise. This problem can be solved by several methods proposed in the literature. One is to use a higher sampling frequency, while another is to implement a synchronous sampling [18]. These approaches increase the computational burden on the digital signal processor and have the disadvantage of implementation complexity. Therefore, in this article, carrier-based SS is adopted to compensate for the voltage phase angle error with limited and fixed sampling frequency [12], [19], [20].

There are two types of carriers used in digital control: sawtooth carrier and triangular carrier. Utilizing triangular carrier-based SS leads to voltage phase angle errors, as depicted in

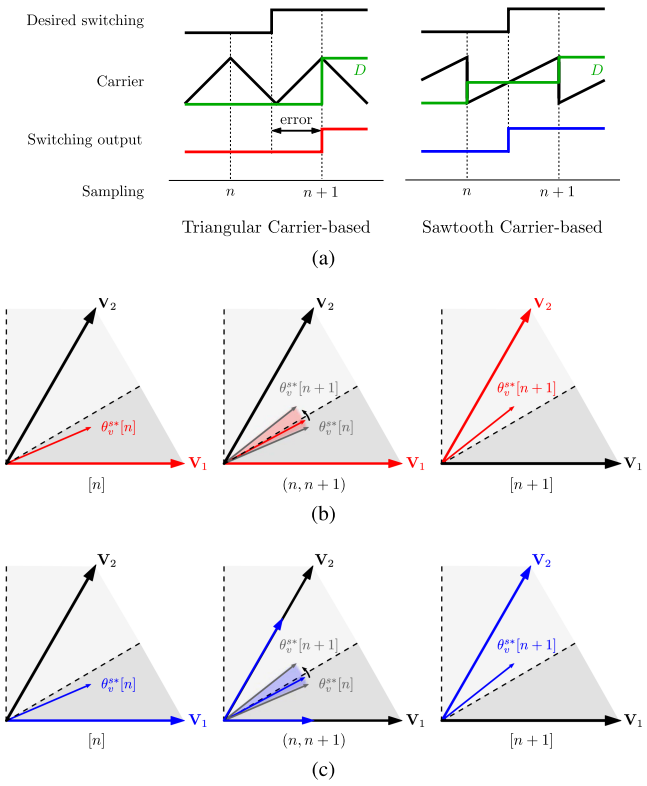

Fig. 7. Implementation of carrier-based six-step operation. (a) Existence of phase angle error depending on carrier. (b) Output voltage vector with triangular carrier. (c) Output voltage vector with sawtooth carrier.

Fig. 7(a) and (b), where duty cycle updating and sampling occur at the peak. In the figure, θ_v^{s*} is the output voltage vector phase angle reference, whose value is defined by

$$\theta_v^{s*} = \theta_r + \arctan(v_{qs}^{r*}, v_{ds}^{r*}). \tag{4}$$

On the other hand, employing the sawtooth carrier, as illustrated in Fig. 7(a) and (c), one can accurately calculate the time for applying the voltage vector and apply it with the duty D. This approach enables the utilization of PWM in SS to apply a voltage vector without voltage phase angle error, even at a fixed sampling frequency.

B. Mode Transition

In the proposed method, there are three operating modes depending on the output voltage vector magnitude. Light load efficiency, which is important in home appliances, should not be worse than that achieved with conventional operation. Therefore, in the proposed method, LM is performed at low speeds to adhere to light-load efficiency. Thereby, accurate voltage synthesis is possible in the LM operating region such that degradation of motor efficiency due to harmonic currents can be avoided. Furthermore, if the SS proposed in Section III-A is applied, accurate voltage synthesis is possible even in the SS region. However, a gap remains between the two operating modes, which can be overcome by using OVM. A detailed description of OVM is given in Section III-C. By applying LM, OVM, and proposed SS, the inverter can accurately synthesize the motor voltage for all operating areas.

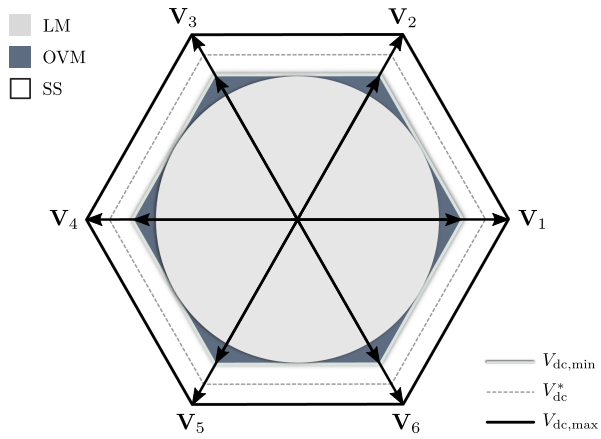

Fig. 8. Operation mode of the proposed control method.

Fig. 8 shows the inverter output voltage vector region of each modulation method. In the figure, a blue hexagon represents the voltage hexagon when the dc-link voltage is $V_{\mathrm{dc,min}}$, and a black hexagon represents that when the dc-link voltage is $V_{\mathrm{dc,max}}$. The dq-axis voltage reference magnitude determines the operation mode, $|v_{dqs}^{r*}|$, which is represented by the mode selector in Fig. 6. The criteria for determining the operation mode are as follows:

$$\text{LM} \quad : |v_{dqs}^{r*}| < \frac{1}{\sqrt{3}} V_{\mathrm{dc,min}} \tag{5}$$

$$\text{OVM} \quad : \frac{1}{\sqrt{3}} V_{\mathrm{dc,min}} \le |v_{dqs}^{r*}| < \frac{2}{\pi} V_{\mathrm{dc,min}} \tag{6}$$

$$\text{SS} \quad : |v_{dqs}^{r*}| \ge \frac{2}{\pi} V_{\mathrm{dc,min}}. \tag{7}$$

When $|v_{dqs}^{r*}|$ meets the criteria of (5), the inverter operates in LM, and the output voltage vector is positioned within the gray area of the voltage hexagon. Similarly, if $|v_{dqs}^{r*}|$ complies with the conditions specified in (6), the inverter switches to OVM, and the output voltage vector is positioned within the blue area. With an increase in $|v_{dqs}^{r*}|$, the inverter transitions to SS, wherein the output voltage vector is chosen from among $\mathbf{V_1}$ to $\mathbf{V_6}$. When implementing mode transition, a hysteresis band is set to ensure a smooth transition and to prevent toggling between modulation methods caused by a dc-link voltage oscillating in the second-order harmonic of the grid voltage, which is natural in a single-phase system.

C. Overmodulation Method

Accurate voltage synthesis from zero speed to rated speed is essential for a smooth transition of different modes in terms of closed-loop current control. Note that inverter output voltage is synthesized accurately with the reference voltage, which is the output of the current controller in both LM and SS with the proposed implementation method presented in Section III-A. The maximum magnitude of the voltage synthesized in LM is $(1/\sqrt{3})V_{\mathrm{dc,min}}$, and the minimum magnitude of the voltage synthesized in SS is $(2/\pi)V_{\mathrm{dc,min}}$. If only two operation modes

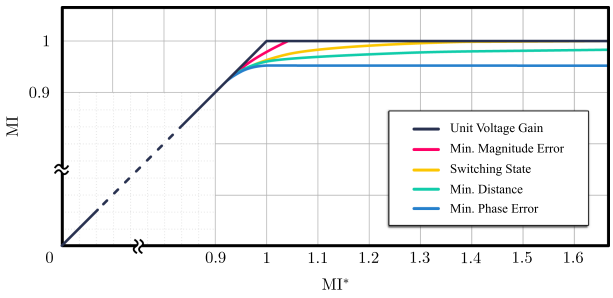

Fig. 9. MI versus MI* curve with different overmodulation methods.

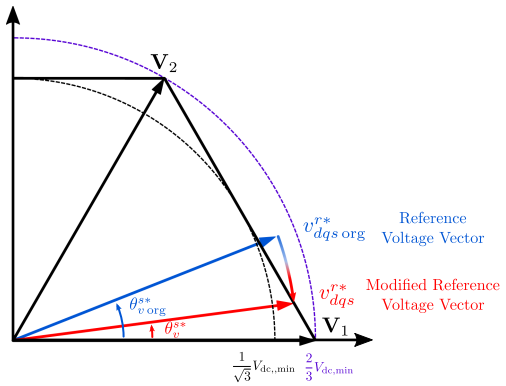

Fig. 10. Implementation scheme of minimum magnitude error method.

are used, the synthesized voltage changes in steps, which causes undesirable instantaneous control failure of the motor current. To bridge this gap region, it is essential to implement OVM to avoid voltage synthesis errors. Therefore, a seamless mode transition is achievable with a single CC since LM, OVM, and SS all match the fundamental components of the CC output voltage and the actual synthesized output voltage.

Several existing OVM methods have been proposed in the literature. Fig. 9 shows the relationship of MI and MI* of the commonly in-use OVM methods [16]. MI is defined as follows:

$$\mathrm{MI} = \frac{V_{\mathrm{s1}}}{\frac{2}{\pi}V_{\mathrm{dc}}}. \tag{8}$$

In the equation, V_{s1} represents the fundamental component of inverter output voltage, and $(2/\pi)V_{\mathrm{dc}}$ is the maximum value of V_{s1} attained by the SS. Switching-state OVM, minimum distance OVM, and minimum phase error OVM either take a long time for MI to reach close to unity or saturate before reaching unity. Accordingly, the OVM method adopted is the minimum magnitude error method, given that it converges to SS the fastest and has the highest linearity among the OVM methods [21].

Fig. 10 shows the voltage hexagon when the dc-link voltage is $V_{\mathrm{dc,min}}$. Within the figure, the lower and upper boundaries of (6) are depicted by a black dashed line, representing the inscribed circle of the hexagon, and a purple dashed line, indicating the circumscribed circle of the hexagon, respectively. During OVM, v_{dqs}^{r*} is positioned between the black and purple circles. The operation of OVM is distinguished based on whether v_{dqs}^{r*} is located inside or outside the voltage hexagon. If v_{dqs}^{r*} resides within the voltage hexagon, the reference voltage can be synthesized, and the output voltage will be equal to the reference voltage. On the other hand, if the voltage vector v_{dqs}^{r*} is outside the hexagon, the reference voltage cannot be synthesized. In such instances, a point on the hexagon matching the reference voltage vector in magnitude and having the smallest phase angle difference is selected for output. When v_{dqs}^{r*} is located on the purple circle, representing the upper boundary of OVM, the output voltage vector corresponds to a vertex of the hexagon, indicative of SS. Consequently, the minimum magnitude error method inherently enables a seamless transition between OVM and SS.

TABLE II
PARAMETERS OF EXPERIMENT

Symbol	Parameter	Nominal value
P_{rated}	Rated power	7 kW
v_{grid}	Grid voltage	220 $V_{\mathrm{ll,rms}}$
v_{dc}	DC-link voltage	311–350 V
L_{PFC}	PFC inductance	400 μH
C_{dc}	DC-link capacitance	3300 μF
$f_{\mathrm{sw,PFC}}$	PFC switching frequency	40 kHz
$f_{\mathrm{sw,INV}}$	Inverter switching frequency	8 kHz

TABLE III
PARAMETERS OF TESTED MOTOR

Symbol	Parameter	Nominal value
p	Pole number	6
R_s	Stator resistance	0.31 Ω
L_{ds}	d component of stator self-inductance	5.82 mH
L_{qs}	q component of stator self-inductance	7.25 mH
λ_f	Back electromotive force constant	0.144 V·s

IV. Experimental Results

To validate the proposed method, experiments are conducted on a 7 kW drivetrain of a commercial residential air conditioner. The experimental parameters of the drivetrain system are shown in Table II, and the parameters of the motor are shown in Table III. The experimental set of the drivetrain is shown in Fig. 11.

A. Validation of Proposed Control Method

In the proposed method, the modulation method is selected between LM, OVM, and SS depending on the voltage reference magnitude of the inverter. Unintended transients occur when switching from LM to SS instead of three steps. Fig. 12 depicts the motor control characteristics based on the inclusion in the OVM region. In the waveform, i_{as} stands for the motor phase current and Torque is calculated torque based on measured current. To emulate the compressor load characteristic, torque reference is increased from 3 N · m to 13 N· m with 2 N· m/s slew rate while the motor speed, ω_{rpm} is changed from 1500 to

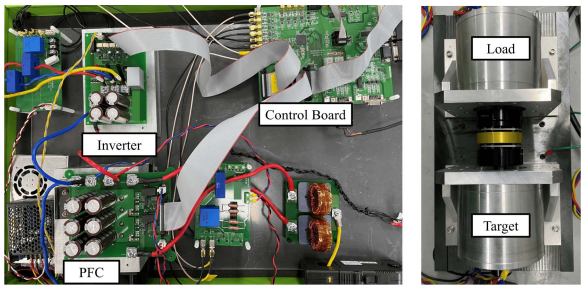

(a) (b)

Fig. 11. Experiment setup. (a) Motor drive system composed of PFC and inverter. (b) Target PMSM and load machine.

4500 r/min with 600 r/min/s slew rate. Fig. 12(a) shows the experimental results when OVM is not adopted. Without OVM, the magnitude of the output synthesized voltage changes abruptly when the modulation method is transited between LM and SS. This causes errors in current control and induces transient torque fluctuation, since the synthesized voltage of SS is $\sqrt{3}\cdot(2/\pi)$ times larger than that of LM. On the other hand, in Fig. 12(b), when OVM is included, the experimental results demonstrate a seamless transition. The zoomed-in waveform of the mode transition instance is shown in Fig. 13, and without OVM, the grid current of the PFC also undergoes a transient response.

The enlarged waveform during mode switching is depicted in Fig. 14. To emulate the compressor load characteristic, the q-axis current reference i_{qs}^{r*} is increased from 5 to 20 A with a slew rate of 3 A/s. Simultaneously, the motor speed $\omega_{\mathrm{r/min}}$ is changed from 1500 to 4500 r/min with a slew rate of 600 r/min/s. The full operation waveform depicts the change in dc-link voltage reference as the mode switches to SS, confirming that the PFC adequately tracks the dc-link voltage reference with sufficient dynamic performance. Because the dc-link voltage of this system contains second-order harmonic components, mode toggling becomes problematic when operated near the transition condition. During the transition between LM and OVM, the voltage reference stays constant at $V_{\mathrm{dc,min}}$ even as the dc-link voltage fluctuates. When transitioning between OVM and SS, mode toggling could be problematic because v_{dc}^{*} is fixed in OVM while v_{dc}^{*} is fluctuating along the dc-link voltage ripple in SS. By employing a hysteresis band, mode toggling and undesired fluctuations caused by dc-link voltage ripple are avoided during mode transitions.

The steady-state waveform of each mode is depicted in Fig. 15. The proposed controller enables both mode switching and steady-state operation at various operating points. In the figure, V_{an} represents the a-phase pole voltage, which is defined as the voltage difference between the motor's a-phase terminal and the dc-link negative terminal. It can be observed from the figure that as the modulation method transits from LM through OVM to SS, the pole-voltage pattern changes in accordance with each modulation. As depicted in Fig. 6, the d-axis compensation current drives the motor into the flux-weakening region when the dc-link voltage reference saturates at $V_{\mathrm{dc,max}}$. Fig. 15(c) illustrates that, upon saturation of v_{dc}^{*} at $V_{\mathrm{dc,max}}$, the d-axis current is regulated to a negative value, resulting in the motor operating within the flux-weakening region. Although current harmonics arise during OVM and SS, as shown in Fig. 15(b) and (c), which can potentially lead to torque ripple, acoustic noise, and reduced efficiency of the motor due to increased iron loss, their effect on the overall system performance of the air conditioner in terms of energy efficiency rating is negligible. This is because such operating modes are only activated instantaneously during high-load conditions, such as the initial startup phase of the air conditioner to rapidly cool down the air. While the system operates predominantly in light-load conditions in the LM region, therefore, the energy efficiency rating of air conditioners is primarily defined by the efficiencies of the inverter and motor in light-load conditions.

B. Grid Current and Harmonic Analysis

Since the application of this controller is an air conditioner connected to the grid, current harmonic regulations for grid connection must be complied with. The experiment set is a single-phase system and is classified as Class A according to IEC 61000-3-2. When operating with the proposed controller, the harmonic components of the grid current are extracted for 20%, 40%, 60%, 80%, and 100% load conditions. The results are shown in Fig. 16. The harmonic regulation value remains satisfied under all load conditions despite the fact that a considerable motor power fluctuation results from the SS. Therefore, the proposed controller can be utilized for grid connection during operation.

C. Power Loss Analysis of Drivetrain System

Applying the proposed control affects both inverter and motor losses. However, for motor losses, the impact is largely confined to the start-up period, which is smaller than the thermal time constant of the motor and constitutes only a small fraction of total operating time. Consequently, the lifetime impact on motor losses is expected to be limited. Accordingly, this section confines its scope to inverter-stage loss analysis.

The total inverter power loss can be categorized into conduction and switching components. The conduction loss, in particular, is defined as follows:

$$P_{\mathrm{cond}} = P_{\mathrm{cond,IGBT}} + P_{\mathrm{cond,FWD}} \tag{9}$$

$$P_{\mathrm{cond,IGBT}} = \frac{1}{T_0}\int_0^{T_0} v_{\mathrm{CE(sat)}}(i_{\mathrm{C}}(t))\cdot i_{\mathrm{C}}(t)\,dt \tag{10}$$

$$P_{\mathrm{cond,FWD}} = \frac{1}{T_0}\int_0^{T_0} v_{\mathrm{F}}(i_{\mathrm{F}}(t))\cdot i_{\mathrm{F}}(t)\,dt \tag{11}$$

where $v_{\mathrm{CE(sat)}}$ and v_{F} represent the collector–emitter saturation voltage of the IGBT and the forward voltage drop of the freewheeling diode, respectively, both as functions of current. i_{C} and i_{F} denote the collector current of the IGBT and the diode current, and T_0 is the period of one fundamental current cycle.

A distinctive feature of the proposed control method is its ability to significantly reduce switching losses under high-load conditions. To validate this effect, the total inverter loss was experimentally measured using a high-precision power analyzer (YOKOGAWA WT5000), which was connected as close as

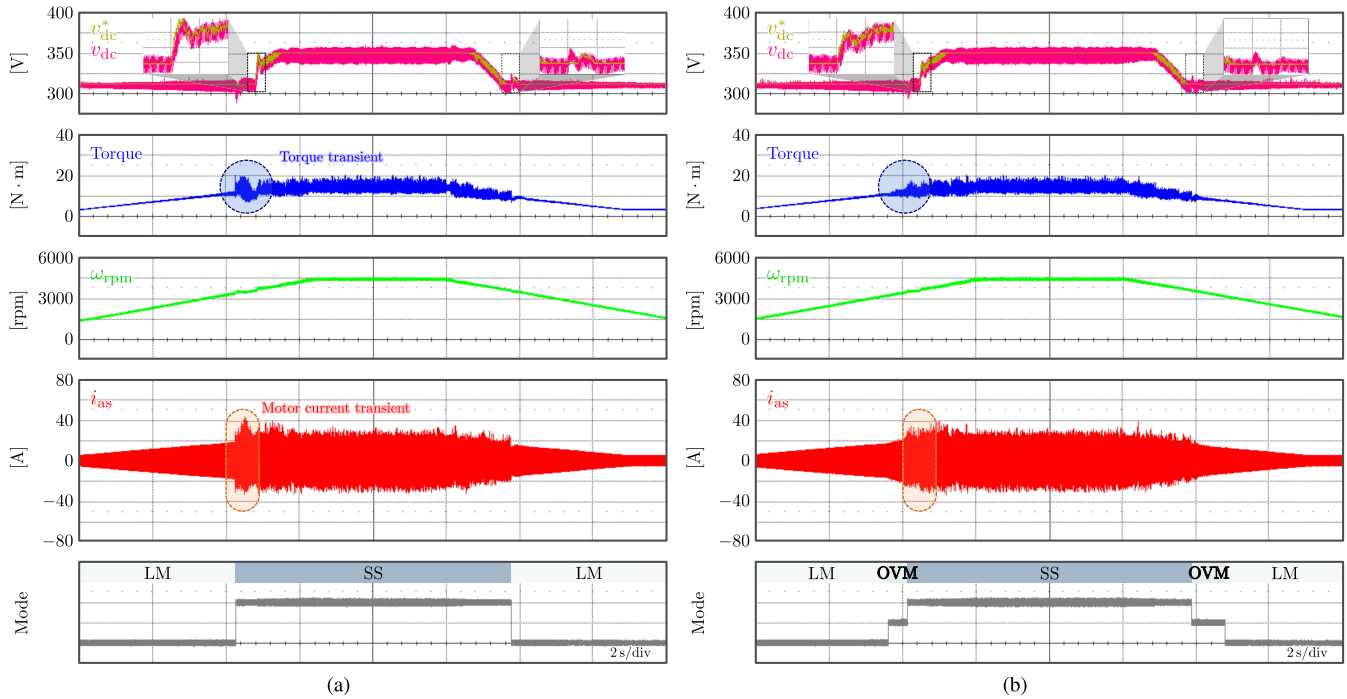

Fig. 12. Experimental results of full range operation. (a) Without OVM. (b) With OVM.

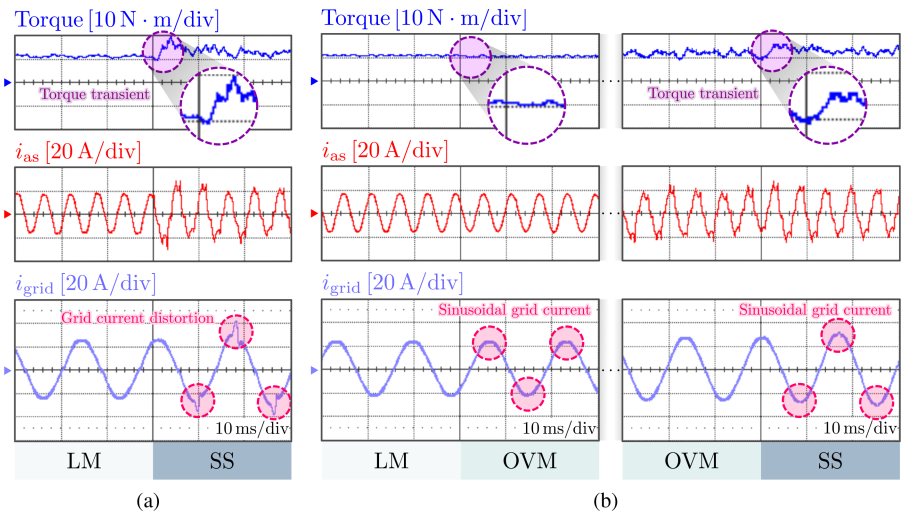

Fig. 13. Zoomed waveform of operating mode transition. (a) Without OVM. (b) With OVM.

possible to the dc-link input and three-phase output terminals to minimize measurement uncertainty. Assuming that the total inverter loss consists only of conduction and switching components, a hybrid approach combining measurement and preobtained V–I characteristic curve was used to perform an accurate loss breakdown. Specifically, the input gate signals and output phase currents of the inverter were recorded to reconstruct the instantaneous conduction intervals of the power semiconductor devices. Conduction loss was then computed based on the measured current waveforms, input gate signals, and the V–I characteristics of the devices during these intervals. The collector–emitter saturation voltage $v_{CE(sat)}$ of the IGBT, which was not provided in the datasheet for the experimental device (Onsemi FNB35060 T), was characterized experimentally by applying a range of collector currents and measuring the corresponding voltages. For the freewheeling diode, the forward voltage v_F was obtained directly from the datasheet. The switching loss was finally determined as the residual between the measured total inverter loss and the calculated conduction loss.

The resulting loss breakdown is presented in Fig. 17. For the conventional control method, LM and OVM based on minimum distance error method are adopted. To ensure a fair comparison, the dc-link voltage reference in both methods was set identically at each load condition. Up to 40% load, both the conventional and proposed methods operate in the LM region, resulting in similar loss levels. In this region, the proposed method

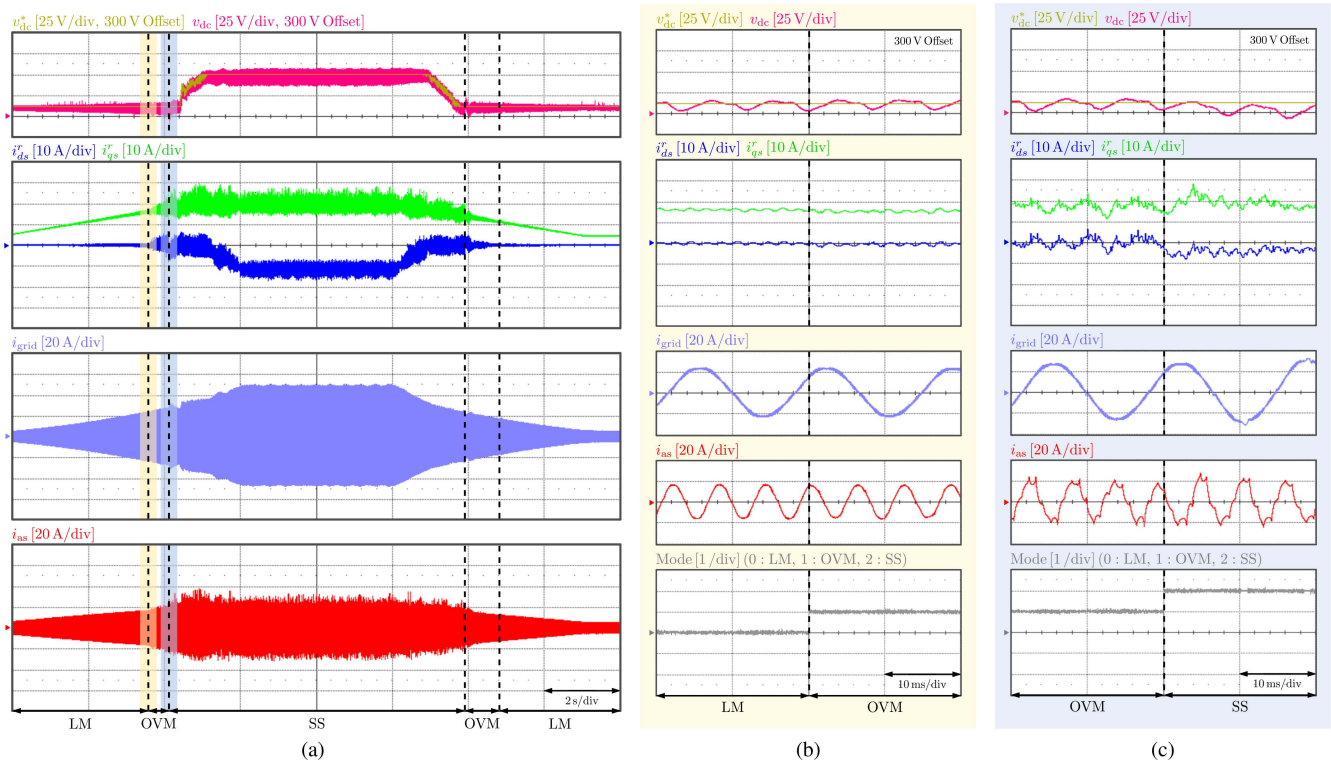

Fig. 14. Experimental results of varying speed and current conditions with OVM. (a) Full range operation. (b) Zoomed-in waveform of LM to OVM. (c) Zoomed-in waveform of OVM to SS.

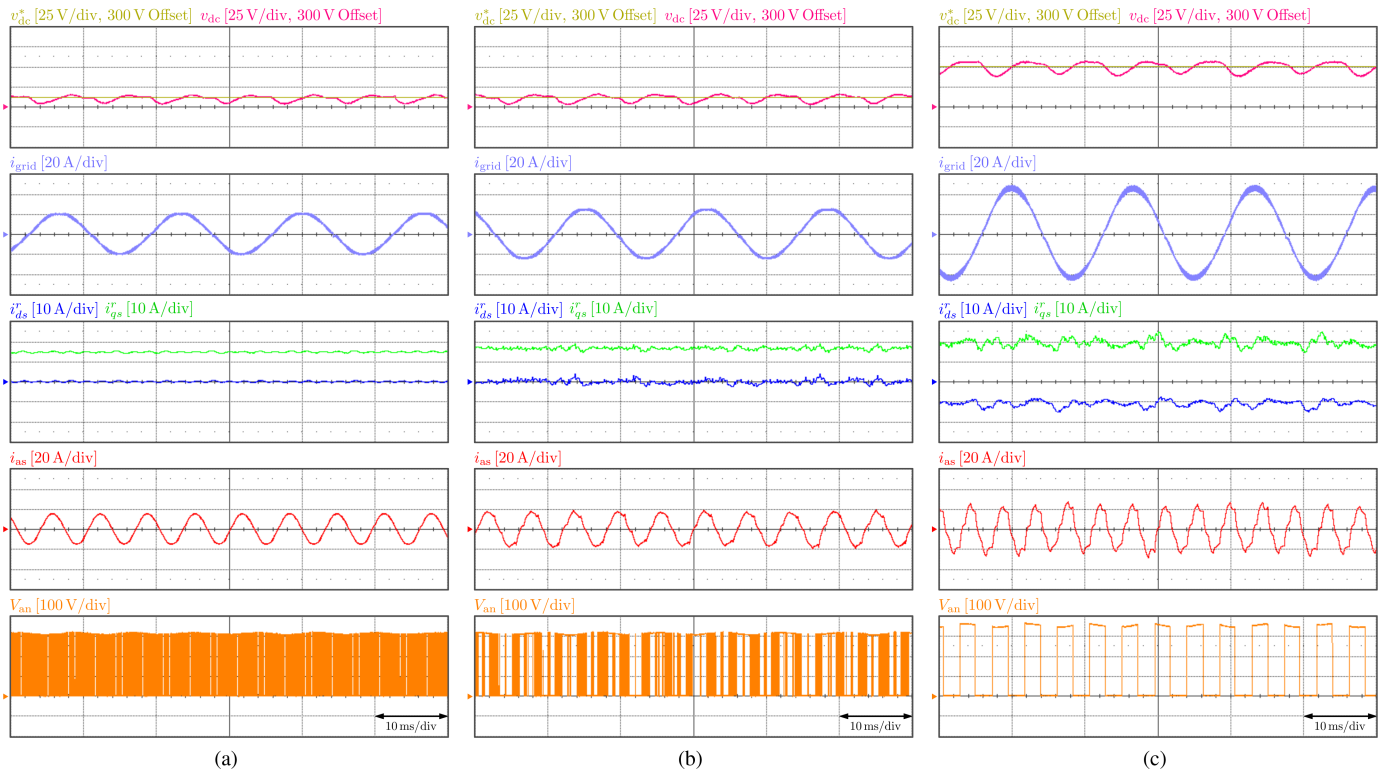

Fig. 15. Experimental results of the steady-state waveform of each mode. (a) LM. (b) OVM. (c) SS.

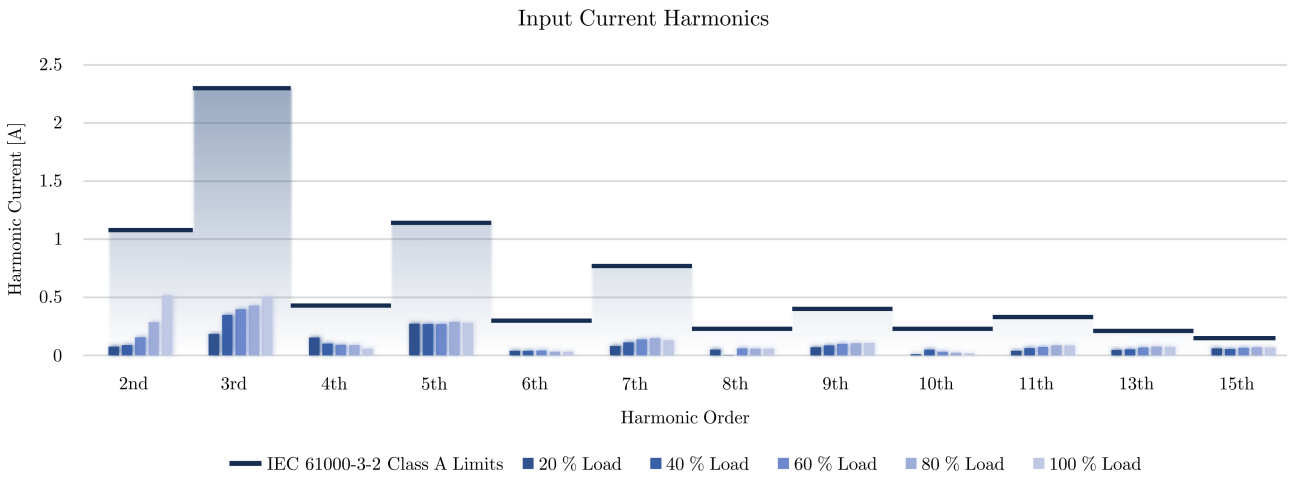

Fig. 16. PFC current harmonic components with proposed control method.

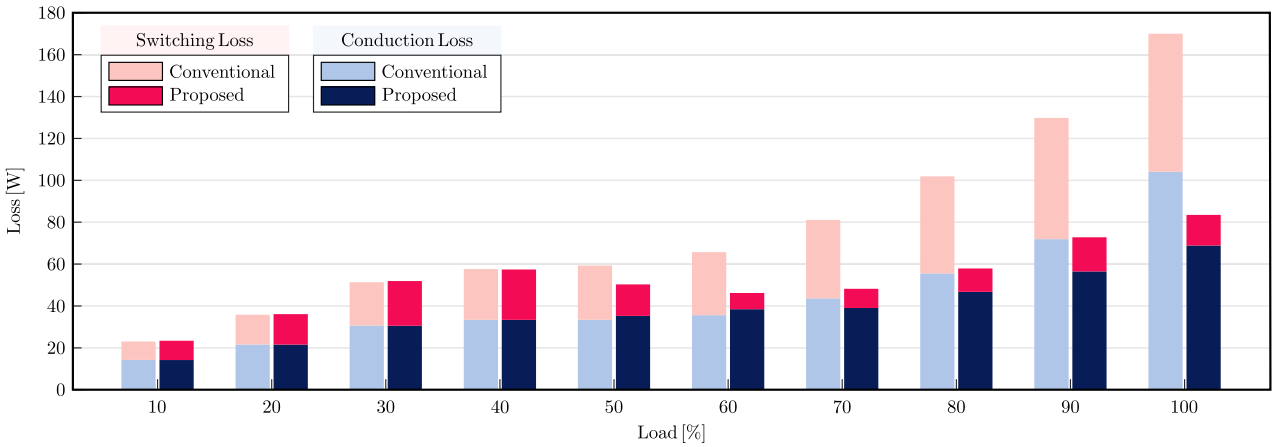

Fig. 17. Power losses of the inverter obtained by experiment under different load points.

intentionally follows the conventional control strategy to maintain high system efficiency under light-load conditions. This is because the switching pattern, phase current, and dc-link voltage are identical, leading to identical inverter behavior and loss characteristics. At 50% load, the conventional method remains in LM, whereas the proposed method transitions to OVM, thereby reducing the switching losses conspicuously. Above 60% load, the conventional method transitions through OVM to FW, while the proposed method transitions through SS before entering FW.

The measurements confirm that under high-load conditions, the proposed method significantly reduces not only switching losses but also conduction losses, as illustrated in Fig. 17. This notable reduction in conduction loss can be attributed to the lower rms phase current observed during FW in the proposed method. Unlike LM, which requires significant negative d-axis current injection to maintain the voltage constraint within the limited modulation range, SS increases voltage utilization margin (0.577 versus 0.637 p.u.). This increased voltage utilization margin relaxes the demand of demagnetizing current for FW and allows the torque-producing q-axis current to be maintained with a smaller total current magnitude [22]. Given the stator inductance values of $L_{ds} = 0.23$ p.u. and $L_{qs} = 0.29$ p.u. of the investigated motor used in residential commercial air conditioners, the increased voltage margin reduces the required d-axis current, resulting in approximately 5%–8% lower total stator current magnitude. In addition, since the conduction loss is not linear with respect to current due to the nonlinear behavior of $v_{\mathrm{CE(sat)}}(i_C)$, the reduction in current is augmented. This nonlinearity further accentuates the conduction loss difference between the proposed and conventional methods under high-load conditions. This theoretical interpretation is consistent with the experimental results, validating the efficiency benefits of the proposed control method under high-load conditions.

Furthermore, the effectiveness of the proposed control method was experimentally validated with the complete drivetrain system that consists of power conversion stage and motor. To this end, the efficiencies of the power conversion stage (PFC+inverter) was measured under both the conventional and proposed control methods. The power conversion stage efficiency is compared in Fig. 18, while the corresponding power loss comparison at rated power is presented in Fig. 19. As the rotational speed ω_r increases, the operation mode switches to the SS, resulting in a significant reduction in switching losses and a corresponding improvement in overall efficiency. This

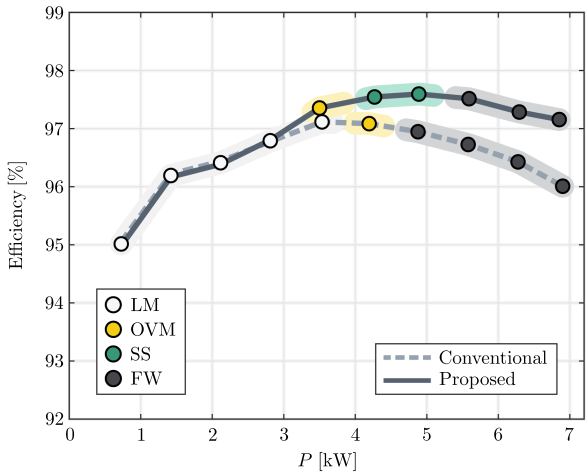

Fig. 18. Efficiency of power conversion (PFC+inverter) under the conventional and proposed control methods.

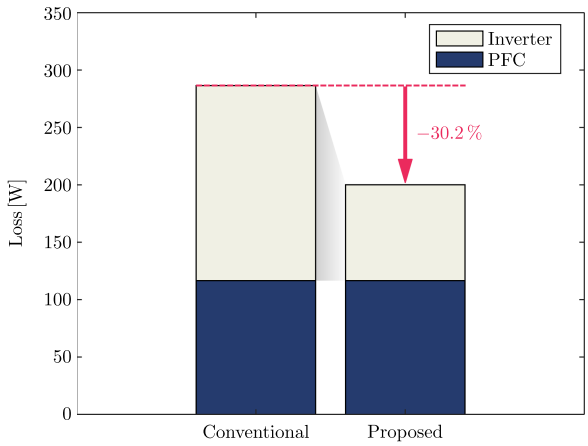

Fig. 19. PFC and inverter loss comparison between conventional and proposed control methods at 7 kW.

effect becomes particularly pronounced near the rated operating point. At rated output power, while the PFC losses remained similar for both methods, the inverter losses under the proposed control were significantly lower, resulting in an overall loss reduction of approximately 30.2%. This confirms that the proposed method primarily reduces power losses through inverter loss reduction, without degrading the efficiency of the PFC stage. These results confirm that the proposed control method enables efficient operation under light-load conditions without performance degradation, and achieves notable inverter loss reduction under high-load conditions due to decreased switching losses. Consequently, the proposed approach effectively reduces heatsink volume and enhances the overall power density of the system, as experimentally verified.

To comprehensively evaluate the inverter performance, three key metrics—efficiency, rms phase current including THD, and total power loss—were compared under rated output conditions and summarized in Table IV with experimental results on a 7 kW commercial air conditioner. The proposed method significantly reduced inverter losses, leading to an improved peak efficiency

TABLE IV
COMPARISON OF INVERTER PERFORMANCE METRICS BETWEEN CONVENTIONAL AND PROPOSED CONTROL METHODS

Method	Peak Efficiency	Phase Current (THD)	Maximum Power Loss
Conventional	98.46%	21.7 A (6.3%)	170 W
Proposed	99.02%	18.3 A (12.1%)	83.5 W

of 99.02%, compared to 98.46% in the conventional method. This improvement is largely attributed to lower rms phase current in the SS (18.3 A) compared to LM (21.7 A), despite a higher THD. This current reduction is a direct consequence of higher voltage utilization in SS. Specifically, the voltage utilization ratio increases, enabling torque to be maintained with smaller current magnitudes under FW conditions. In contrast, LM requires deeper FW and higher rms current, due to both its lower MI and additional voltage margin reserved to ensure modulation linearity. The tested motor, which has a relatively high flux linkage λ_f, further amplifies this difference by demanding greater weakening current in the LM case. Therefore, the observed difference in rms phase current is not only consistent with theoretical expectations but also amplified by the design of the motor and controller. Despite SS increases current THD, the experimental data highlight the suitability of the proposed control method for systems prioritizing inverter-side loss reduction, especially in the high-load regime.

V. CONCLUSION

This article proposes a control method designed to minimize peak power loss of switching devices in the residential air conditioner utilizing adjustable dc-link voltage and SS. A coordinated control method coupled with variable dc-link voltage and SS in a two-stage power conversion system is proposed. This is achieved through coordinated control of the PFC and the inverter. With variable dc-link voltage SS, accurate voltage synthesis is possible even in SS, and losses are reduced compared to conventional operation at the rated operating point. Two control degrees of freedom, dc-link voltage and phase angle of the voltage vector, allow independent control of the dq-axis current in a closed loop. This not only enhances robustness against motor parameter errors but also enables MTPA operation by taking advantage of closed-loop current control for the LM, OVM, and SS regions. Moreover, utilizing SS at the high speed of the motor ensures a minimal magnitude of the d-axis current, which is crucial for flux-weakening operation. However, a challenge arises when SS is employed at low speed, as the fixed magnitude of the synthesized voltage can impact efficiency at light loads. To address this challenge, the proposed method employs LM at light loads but seamlessly transits to SS with minimum magnitude error OVM as the rotational speed increases. This mode transition depending on the load condition of the motor allows for reduced switching device losses at rated operating points without compromising efficiency at light loads. Experimental validation confirms that the proposed method can achieve significant loss reduction at rated power without compromising efficiency at light loads.

Nevertheless, one remaining step is required for product-level deployment. Appliance inverters are constrained by cost to a

single-shunt current sensor. Although single-shunt sensing is feasible with conventional space-vector modulation, in SS the measurement window collapses at the six vertices of the voltage hexagon, leaving intervals in which the phase currents cannot be reconstructed. Therefore, developing and validating a low-cost current sensing scheme usable in SS is identified as key future work toward full product deployment.

REFERENCES

[1] D. Vérez, E. Borri, and L. F. Cabeza, "Trends in research on energy efficiency in appliances and correlations with energy policies," *Energies*, vol. 15, no. 9, 2022, Art. no. 3047.

[2] I. E. Agency, *The Future of Cooling: Opportunities for Energy-Efficient Air Conditioning.* Paris, France: International Energy Agency, 2018.

[3] K. Tsukii, M. Tamura, W. Hatsuse, and Y. Notohara, "Improvement of system efficiency by variable switching frequency control for converter," in *Proc. Power Electron. Conf.*, 2022, pp. 673–677.

[4] A. Gomes, C. H. Antunes, and J. Martinho, "A physically-based model for simulating inverter type air conditioners/heat pumps," *Energy*, vol. 50, pp. 110–119, 2013.

[5] T. Schoenen, M. S. Kunter, M. D. Hennen, and R. W. De Doncker, "Advantages of a variable DC-link voltage by using a DC-DC converter in hybrid-electric vehicles," in *Proc. IEEE Veh. Power Propulsion Conf.*, 2010, pp. 1–5.

[6] P. Pescetto, A. Sierra-Gonzalez, F. Alvarez-Gonzalez, H. Kapeller, E. Trancho, and G. Pellegrino, "Active control of variable DC-link for maximum efficiency of traction motor drives," *IEEE Trans. Ind. Appl.*, vol. 59, no. 4, pp. 4120–4129, Jul./Aug. 2023.

[7] S. Tenner, S. Gimther, and W. Hofmann, "Loss minimization of electric drive systems using a DC/DC converter and an optimized battery voltage in automotive applications," in *Proc. IEEE Veh. Power Propulsion Conf.*, 2011, pp. 1–7.

[8] T.-S. Li, Y.-H. Yang, C.-A. Cheng, and Y.-M. Chen, "A variable DC-link voltage determination method for motor drives with sic mosfets," in *Proc. IEEE Workshop Wide Bandgap Power Devices Appl. Asia (WiPDA Asia)*, 2020, pp. 1–6.

[9] H. S. Park, M. Kim, and B. K. Lee, "Light load efficiency improvement in variable DC-link voltage inverter systems for home appliances," *J. Elect. Eng. Technol.*, vol. 11, no. 5, pp. 1274–1281, 2016.

[10] J. Yun, Y.-K. Son, and S.-K. Sul, "Parallel operation of permanent magnet synchronous generators under six-step operation mode," in *Proc. IEEE Transp. Electrific. Conf. Expo*, 2022, pp. 635–639.

[11] A. M. Hava, R. J. Kerkman, and T. A. Lipo, "Carrier-based PWM-VSI overmodulation strategies: Analysis, comparison, and design," *IEEE Trans. Power Electron.*, vol. 13, no. 4, pp. 674–689, Jul. 1998.

[12] J. Yun, Y.-K. Son, H.-J. Cho, and S.-K. Sul, "DC bus voltage regulation strategy in maritime DC power system for minimized converter loss," *IEEE Trans. Power Electron.*, vol. 36, no. 11, pp. 13225–13233, Nov. 2021.

[13] I. Ralev, T. Lange, and R. W. De Doncker, "Wide speed range six-step mode operation of IPMSM drives with adjustable DC-link voltage," in *Proc. 17th Int. Conf. Elect. Machines Syst.*, 2014, pp. 2987–2993.

[14] H.-Y. O. Yang and R. D. Lorenz, "Torque ripple minimization in six-step PMSM drives via variable and fast DC bus dynamics," *IEEE Trans. Ind. Appl.*, vol. 55, no. 4, pp. 3791–3802, Jul./Aug. 2019.

[15] J. Ham, H. Kim, J. Maeng, and S. Cui, "Vector control of AC motor in six-step operation based on variable DC-link voltage," in *Proc. IEEE Appl. Power Electron. Conf. Expo.*, 2024, pp. 143–147.

[16] Y.-C. Kwon, S. Kim, and S.-K. Sul, "Six-step operation of PMSM with instantaneous current control," *IEEE Trans. Ind. Appl.*, vol. 50, no. 4, pp. 2614–2625, July–Aug. 2014.

[17] S.-K. Sul, *Control of Electric Machine Drive System*. Oxford, U.K.: IEEE Press, 2011.

[18] J. Park, S. Jung, and J.-I. Ha, "Variable time step control for six-step operation in surface-mounted permanent magnet machine drives," *IEEE Trans. Power Electron.*, vol. 33, no. 2, pp. 1501–1513, Feb. 2018.

[19] H.-J. Cho, Y.-C. Kwon, and S.-K. Sul, "Time-optimal voltage vector transition scheme for six-step operation of PMSM," *IEEE Trans. Power Electron.*, vol. 36, no. 5, pp. 5724–5735, May 2021.

[20] Z. Ke, J. Zhang, and R. Raich, "Low-frequency current oscillation reduction for six-step operation of three-phase inverters," *IEEE Trans. Power Electron.*, vol. 32, no. 4, pp. 2948–2956, Apr. 2017.

[21] S. Bolognani and M. Zigliotto, "Novel digital continuous control of SVM inverters in the overmodulation range," *IEEE Trans. Ind. Appl.*, vol. 33, no. 2, pp. 525–530, Mar.–Apr. 1997.

[22] S.-Y. Jung, C. C. Mi, and K. Nam, "Torque control of IPMSM in the field-weakening region with improved DC-link voltage utilization," *IEEE Trans. Ind. Electron.*, vol. 62, no. 6, pp. 3380–3387, Jun. 2015.

Jisun Ham (Student Member, IEEE) received the B.S. degree in electrical engineering from Ajou University, Suwon, South Korea, in 2021. She is currently working toward the Ph.D. degree in electrical engineering with Seoul National University, Seoul, South Korea.

Her research interests include applications of wide-band gap power devices, cryogenic power electronics, and control of grid-connected converters.

Hwigon Kim (Member, IEEE) received the B.S. and Ph.D. degrees in electrical engineering and computer science from Seoul National University, Seoul, South Korea, in 2018 and 2023, respectively.

From 2023 to 2024, he was a Postdoctoral Researcher with the Electric Power Research Institute, Seoul National University. He is currently a Senior Motor Control Engineer with Rivian, LLC, Irvine, CA, USA. His current research interests include the control of power electronics and its application to electrical machines.

Junyeol Maeng (Student Member, IEEE) received the B.S. degree in electrical and computer engineering in 2022 from Seoul National University, Seoul, South Korea, where he is currently working toward the Ph.D. degree in electrical and computer engineering.

His research focuses on wide-bandgap power semiconductor devices, modeling and application in power conversion, and control of grid-forming converters.

Shenghui Cui (Member, IEEE) received the B.S. degree from Tsinghua University, Beijing, China, in 2012, the M.S. degree from Seoul National University, Seoul, South Korea, in 2014, and the Dr.-Ing. degree with the highest distinction (*summa cum laude*) from RWTH Aachen University, Aachen, Germany, in 2019, all in electrical engineering.

Since September 2021, he has been with the Department of Electrical and Computer Engineering, Seoul National University, Seoul, South Korea, where he is currently an Associate Professor. From March 2015 to May 2021, he has been with the Institute for Power Generation and Storage Systems, E.ON Energy Research Center, RWTH Aachen University, where he was a Research Associate and later on Senior Scientist. His research interests include interaction of power systems and power converters, high-power converters in ac and dc utility applications (e.g., HVDC, FACTS, and SSTs), control and power hardware-in-the-loops, high-power ac drives for shipboard propulsions, applications of wide-band gap power devices, and cryogenic power electronics.

Dr. Cui was the recipient of the STAWAG Best Dissertation Prize from Faculty of Electrical Engineering and Information Technology, RWTH Aachen University in 2019, the Second Place Prize Paper Award of IEEE TRANSACTIONS ON POWER ELECTRONICS in 2018, and Best Paper Award of IEEE PEDG in 2025, the Second Prize Paper Award of IEEE IPEC (ECCE Asia) in 2018, and the Outstanding Presentation Award of the IEEE Applied Power Electronics Conference in 2014.